TECHNISCHE MECHANIK, 32, 2-5, (2012), 342 – 357
submitted: November 2, 2011

Mechanical Behavior of Mushy Zone in DC casting using a Viscoplastic Material Model

P. Pavan Kumar, A. K. Nallathambi, E. Specht, A. Bertram

Direct Chill (DC) casting is a semi-continuous metal manufacturing process for producing non-ferrous alloys such as aluminum and magnesium. During the solidification of the alloy, there exists a semi-solid state of material known as mushy zone which is more prone to hot tearing. Precise modeling of hot tearing is the most challenging task due to the interaction of many physical fields. The deformation of the partially coherent solid strongly influences the hot cracking. This work focuses on the material behavior of the mushy zone which is the prerequisite for the development of hot tearing criteria. The rate-dependent nature plays a crucial role at higher temperatures. Therefore, the viscoplastic material models with temperature-dependent coefficients are implemented for the characterization of the mushy zone. The numerical integration of the constitute equations are explained in detail. The liquid flow is neglected, and the momentum and energy equations are solved for the mushy and solid phases. With the help of a viscoplastic material models, the stress and strain evolution in the mushy zone is captured. It is found that the state of stress in mushy region is tensile in nature which is a favorable situation for the hot cracks. The influence of the casting speed and secondary cooling on the mushy stress state are analyzed in detail.

1 Introduction

The complete DC casting process can be divided into three stages: (a) start-up phase, (b) pseudo steady-state, and (c) end phase. In the start-up phase, the bottom block lies inside the mold, and the liquid metal is poured from the top through a distribution bag into the bottomless mold. The level of liquid metal is maintained constant in the mold by means of continuous addition of liquid metal. The mold is supplied by a cooling water which is known as primary cooling. The liquid metal rejects heat through metal-mold and metal-bottom block interaction. A solidified shell is formed over the bottom block and along the mold wall. As soon as the solidified shell is strong enough to support the molten metal inside, the bottom block is lowered with certain velocity .This sequence of processes are known as start-up phase. At the exit of the mold, cooling water directly touches the billet, known as secondary cooling. When the cooling water directly touches the surface of the billet, the solidification process becomes accelerated. After the start-up phase, a pseudo steady-state is reached during which the thermal and mechanical field quantities reach constant values. In general, during this phase the velocity of the bottom block is maintained constant. This phase is almost steady in time. At last, the liquid metal feeding and the movement of bottom block are stopped and the billet is kept for a certain time so that there is no liquid or semi-solid material left. This phase is known as the end phase. Both the start-up and end phase are transient in nature.

The simulation of phase-change problems is highly important for achieving a high quality casting and to avoid difficult experiments. During the phase-change, the latent heat release introduces a severe non-linearity and a local exchange of the field variables. Celentano et al. (1994) proposed a temperature-based FEM for the phase-change problem which incorporates the latent heat release by means of an additional phase-change matrix and a latent heat vector. Fachinotti et al. (1999) followed the COO's temperature formulation and introduced an element split technique along with a line-search algorithm. Nallathambi et al. (2009) attempted to extend the suitability of the temperature-based formulation even for high Stefan numbers.

It is mandatory to know the history of the residual stress-strain development at every material point for the prediction of cracks. Further, the rate-dependent effects dominate in high temperature regions. Therefore, the mechanical behavior of the ingot is described by an elastic-viscoplastic material model. Fjær and Mo (1990) presented a DC casting mathematical model using the finite element method. They demonstrated the numerical method for computing the stress and strain using an axisymmetric circular billet. Drezet and Rappaz (1996) and Katgerman et al. (1990) significantly contributed in the field of DC casting modeling. Williams et al. (2003) simulated the 3-D DC

casting of AA1201 alloy using a commercial package ANSYS. They used a modified Perzyna type viscoplastic law for the prediction of the mechanical behavior of the solid and the mushy phases. Material hardening effects and the initial free surface filling are not included in their model. They reported extremely high values of stresses due to the inappropriate material model. Therefore, it is important to incorporate a proper material model. Magnin et al. (1996) performed tensile tests on an Al–4.5%Cu alloy in order to determine the rheology and ductility over a wide range of temperature moving from room temperature to the dendiritic coherency temperature. Based on their experminetal observations they proposed an elasto-viscoplastic law. Suyitno et al. (2004) used the same law for the solid phase and proposed a different constitutive law for the mushy phase which is similar to the Garafalo law. However, they incorporated the solid fraction in the constitutive law of the mushy phase which is not the case for the Garafalo law. Drezet and Rappaz (1996) used the Garafalo law for the solid phase and Norton-Hoff law for the mushy phase. They investigated the AA1201 alloy and predicted the butt curl, butt swell, and rolling faces inward pull-in. M'Hamdi et al. (2003) used a complex viscoplastic law with more material parameters. In this work, the liquid phase is treated as a fictitious solid with a very small stiffness since it can not accommodate stresses. Within the mushy zone, there is a coherency point where the material starts sustaining the mechanical loads. From the coherency temperature to the solidus temperature, the mechanical behavior of the material is modeled by Norton's viscoplastic law. The solid phase is assumed to behave according to Garafalo's viscoplastic law. With these models, the stress-strain development near the mushy zone is carefully studied. The detailed literature review can be found in Nallathambi et al. (2009).

2 Thermal Field

The energy balance for the phase-change heat conducting body can be derived based on the heat capacitance method as (Nallathambi et al., 2009),

$$\nabla \cdot (k \nabla \theta) \; + \; \rho \, r_q \; = \; \rho \left(C_p \; + \; L \, \frac{\partial f_{pc}}{\partial \theta} \right) \dot{\theta} \tag{1}$$

where k is the thermal conductivity, θ is the temperature, ρ is the density, r_q is the heat generation, C_p is the specific heat, L is the latent heat, and f_{pc} is the phase fraction. A linear phase-change function is assumed in the mushy region. A temperature-based fixed grid finite element method (Celentano et al., 1994) yields the following final form as

$$\mathbf{K} \, \Theta \; + \; \mathbf{C} \, \dot{\Theta} \; + \; \dot{\mathbf{L}} \; = \; \mathbf{F} \tag{2}$$

where **K** is the thermal conductance matrix, **C** is the capacitance matrix, **L** is the latent heat vector, **F** is the force vector, and Θ is the nodal temperature vector. Further details about the numerical method can be found in Nallathambi et al. (2009).

3 Mechanical Field

Small deformation theory is used to model the mechanical behavior of the ingot. The contribution of the metal shrinkage during solidification is neglected due to the constant liquid feeding within the mushy zone. The alloy is allowed to contract as soon as it reaches the coherency temperature (Drezet and Rappaz, 1996). The linear momentum balance for the deforming body can be given as

$$\nabla \cdot \mathbf{T} \; + \; \vec{b}_f \; = \; \vec{0} \tag{3}$$

subject to the boundary conditions

$$\vec{u} = \vec{u}_s \tag{4}$$

$$\mathbf{T} \cdot \vec{n} = \vec{t}_f \tag{5}$$

where **T** is the Cauchy stress tensor, $\vec{b}_f$ is the body force vector, $\vec{u}_s$ is the prescribed displacement vector, and $\vec{t}_f$ is the prescribed traction vector with unit outward normal $\vec{n}$.

The total strain **E** can be additively decomposed into three components as

$$\mathbf{E} = \frac{1}{2} \left[\nabla \vec{u} + (\nabla \vec{u} \,)^T \right] = \mathbf{E}^{\mathrm{e}} + \mathbf{E}^{\mathrm{t}} + \mathbf{E}^{\mathrm{vp}} \tag{6}$$

where $\mathbf{E}^{\mathrm{e}}$ is the elastic strain tensor, $\mathbf{E}^{\mathrm{t}}$ is the thermal strain tensor, and $\mathbf{E}^{\mathrm{vp}}$ is the viscoplastic strain tensor. Using

the elastic part of the strain tensor $\mathbf{E}^{\mathrm{e}}$, stress tensor $\mathbf{T}$ can be determined from the elastic law of the material as

$$\mathbf{T} = \mathbb{C} : \mathbf{E}^{\mathrm{e}} \tag{7}$$

where $\mathbb{C}$ is the fourth-order isotropic elasticity tensor defined as,

$$\mathbb{C} \;=\; 3\kappa\,\mathbb{P}_1 \;+\; 2\mu\,\mathbb{P}_2 \tag{8}$$

where κ is the bulk modulus, and μ is the shear modulus which are both functions of temperature and phase fraction. $\mathbb{P}_1$ and $\mathbb{P}_2$ are the fourth-order volumetric and deviatoric projectors respectively, defined as

$$\mathbb{P}_1 \;=\; \frac{1}{3}\,(\mathbf{I}\otimes\mathbf{I}) \tag{9}$$

$$\mathbb{P}_2 \;=\; \mathbb{I} \;-\; \frac{1}{3}\,(\mathbf{I}\otimes\mathbf{I}) \tag{10}$$

where $\mathbf{I}$ is the second-order identity tensor, $\mathbb{I}$ is the fourth-order identity tensor, and $\otimes$ is the tensor product.

The thermal strain tensor is defined as

$$\mathbf{E}^{\mathrm{t}} \;=\; \alpha\,(\theta \;-\; \theta_{ref})\,\mathbf{I} \tag{11}$$

where α is the linearized coefficient of thermal expansion, θ, and θ_{ref} are the current and reference temperatures, respectively.

The viscoplastic strain rate tensor ($\dot{\mathbf{E}}^{\mathrm{vp}}$) can be written in terms of a scalar viscoplastic strain rate ($\dot{\epsilon}^{vp}$) as (Drezet and Rappaz, 1996)

$$\dot{\mathbf{E}}^{\mathrm{vp}} \;=\; \frac{3}{2}\,\dot{\epsilon}^{vp}\,\frac{\mathbf{T}'}{\sigma_{\mathrm{eff}}} \;=\; \dot{\epsilon}^{vp}\,\tilde{\mathbf{N}} \tag{12}$$

where $\tilde{\mathbf{N}}$ is the flow direction, σ_{eff} is the von Mises equivalent stress, and $\dot{\epsilon}^{vp}$ is the equivalent viscoplastic strain rate. The Norton-Hoff law is one of the simplest viscoplastic model. The mechanical behavior of mushy phase can be well modeled by this law.

$$\dot{\epsilon}^{vp} \;=\; \tilde{k}\,\left(\frac{\sigma_{\mathrm{eff}}}{\tilde{\sigma}_o}\right)^{\tilde{n}} \tag{13}$$

where $\tilde{k}$, $\tilde{\sigma}_o$, and $\tilde{n}$ are the temperature-dependent material constants.

In DC casting, the solidified metal behaviour can be well modeled using the Garafalo law

$$\dot{\epsilon}^{vp} \;=\; A\,\left[sinh\left(\frac{\sigma_{\mathrm{eff}}}{\tilde{\sigma}_o}\right)\right]^{\tilde{n}}\;e^{-\left(\frac{Q}{RT}\right)} \tag{14}$$

where A, $\tilde{\sigma}_o$, and $\tilde{n}$ are the material-dependent constants, Q is the apparent creep activation energy, R is the universal gas constant, and T is the absolute temperature.

By using the variational principles, for an arbitrary virtual displacement field $\vec{\tilde{u}}$ the mechanical equilibrium condition Eq. (3) has to satisfy the following integral equation

$$\int_{\Omega}\Big[\;\nabla\cdot\mathbf{T} \;+\; \vec{b}_f\;\Big]\;\cdot\;\vec{\tilde{u}}\;d\Omega \;=\; 0 \tag{15}$$

By integrating the above equations, the final weak form of GDE can be derived as

$$\int_{\Omega}\mathbf{T}\;:\;\tilde{\mathbf{E}}\;\;d\Omega \;=\; \int_{\Gamma_t}\vec{t}_f\;\cdot\;\vec{\tilde{u}}\;d\Gamma_t \;+\; \int_{\Omega}\vec{b}_f\cdot\vec{\tilde{u}}\;d\Omega \tag{16}$$

Following the standard FE technique, the algebraic form of the above equation is

$$\mathbf{K}\,\mathrm{U} \;=\; \mathrm{F} \tag{17}$$

The FE equation is highly nonlinear and can be solved using an iterative scheme in which the total displacement

at the current time-step and the current iteration is

$$\mathrm{U}_{i+1}^{n+1} \;=\; \mathrm{U}_{i}^{n+1} \;+\; \delta\mathrm{U} \tag{18}$$

The final form of mechanical equilibrium equation becomes

$$\mathbf{K}_{i}^{n+1}\,\delta\mathrm{U} \;=\; \mathrm{F}^{n+1} \;-\; \mathrm{R}_{i}^{n+1} \tag{19}$$

The elemental forms of matrices and vectors are given as

$$\mathbf{K}^{e}{}_{i}^{n+1} = \int_{\Omega^e} \left[\, \mathbf{B}^T\, \mathbf{C}^{ep}{}_{i}^{n+1}\, \mathbf{B} \,\right] d\Omega^e \tag{20}$$

$$\mathrm{F}^{e\,n+1} \;=\; \int_{\Gamma_t^e} \left[\, \Psi_e^T\, \mathrm{T}_f^{e\,n+1} \,\right] d\Gamma_t^e \;+\; \int_{\Omega^e} \left[\, \Psi_e^T\, \mathrm{B}_f^{e\,n+1} \,\right] d\Omega^e \tag{21}$$

$$\mathrm{R}^{e}{}_{i}^{n+1} \;=\; \int_{\Omega^e} \left[\, \mathbf{B}^T\, \mathrm{T}^{e}{}_{i}^{n+1} \,\right] d\Omega^e \tag{22}$$

where $\mathbf{K}$ is the global tangent stiffness matrix, F is the global external force vector, R is the global internal force vector, $\mathbf{C}^{ep}$ is the elemental consistent elasto-viscoplastic operator from the previous iteration. The determination of the tangent stiffness matrix, internal reaction vector, and consistent elasto-plastic/elasto-viscoplastic operator demands the integration of elasto-viscoplastic constitutive relations. The fully implicit backward Euler integration scheme is employed for the derivation of the necessary equations. The stress update in the local integration point level is stated as

$$\mathrm{T}^{n+1} \;=\; \mathrm{T}^{n} \;+\; \Delta\mathrm{T} \tag{23}$$

where T^n is the known previous time-step equilibrium stress. The incremental stress $\Delta\mathrm{T}$ can be expressed by the thermo-elasto-viscoplastic constitutive relation as

$$\Delta\mathrm{T} \;=\; \mathbf{C}\left(\Delta\mathrm{E} - \Delta\mathrm{E}^{\mathrm{t}} - \Delta\mathrm{E}^{\mathrm{vp}}\right) \tag{24}$$

The viscoplastic strain can be approximated using the backward Euler time difference and substituting Eq. (12) as

$$\left(\dot{\mathrm{E}}^{\mathrm{vp}}\right)^{n+1} \;=\; \frac{(\mathrm{E}^{\mathrm{vp}})^{n+1} - (\mathrm{E}^{\mathrm{vp}})^{n}}{\Delta t} \;=\; \frac{\Delta\mathrm{E}^{\mathrm{vp}}}{\Delta t} \;=\; (\dot{\epsilon}^{vp})^{n+1}\;\tilde{\mathrm{N}}^{n+1} \tag{25}$$

where $\tilde{\mathrm{N}}$ is flow direction vector. Therefore, the current stress becomes

$$\mathrm{T}^{n+1} \;=\; \mathrm{T}^{n} \;+\; \mathbf{C}\left(\Delta\mathrm{E} - \Delta\mathrm{E}^{\mathrm{t}} \;-\; \Delta t\;(\dot{\epsilon}^{vp})^{n+1}\;\tilde{\mathrm{N}}^{n+1}\right) \tag{26}$$

This equation is implicit in nature, therefore an iterative scheme is adopted. Keeping k as the previous local iteration counter, the residual can be stated as

$$\bar{\mathrm{R}}_{k}^{n+1} \;=\; \mathrm{T}_{k}^{n+1} \;-\; \mathrm{T}^{n} \;-\; \mathbf{C}\left(\Delta\mathrm{E} - \Delta\mathrm{E}^{\mathrm{t}} \;-\; \Delta t\;(\dot{\epsilon}^{vp})_{k}^{n+1}\;\tilde{\mathrm{N}}_{k}^{n+1}\right) \tag{27}$$

Thus, consider a first-order Taylor series expansion of the residual vector

$$\bar{\mathrm{R}}_{k+1}^{n+1} \;=\; \bar{\mathrm{R}}_{k}^{n+1} \;+\; \frac{\partial\bar{\mathrm{R}}_{k}^{n+1}}{\partial\mathrm{T}_{k}^{n+1}}\,d\mathrm{T} \tag{28}$$

where $d\mathrm{T}$ is the local iterative-increment of stress vector at integration point. Forcing $\bar{\mathrm{R}}_{k+1}^{n+1}$ to reach zero

$$d\mathrm{T} \;=\; -\left[\frac{\partial\bar{\mathrm{R}}_{k}^{n+1}}{\partial\mathrm{T}_{k}^{n+1}}\right]^{-1}\;\bar{\mathrm{R}}_{k}^{n+1} \;=\; -\;\bar{\mathbf{K}}^{-1}\,\bar{\mathrm{R}}_{k}^{n+1} \tag{29}$$

where the Jacobian matrix $\bar{\mathbf{K}}$ can be derived from Eq. (27) as

$$\bar{\mathbf{K}} \;=\; \mathbf{I} \;+\; \mathbf{C}\,\Delta t \left(\frac{\partial \dot{\epsilon}^{vp}}{\partial \mathrm{T}}\,\tilde{\mathrm{N}}^{T} \;+\; \dot{\epsilon}^{vp}\,\frac{\partial \tilde{\mathrm{N}}}{\partial \mathrm{T}} \right)_{k}^{n+1} \tag{30}$$

$\dot{\epsilon}^{vp}$, and $\tilde{\mathrm{N}}$ are functions of current local iterative stress vector T_{k}^{n+1}. Therefore

$$\left.\frac{\partial \dot{\epsilon}^{vp}}{\partial \mathrm{T}}\right|_{k}^{n+1} \;=\; \frac{\partial \dot{\epsilon}^{vp}}{\partial \sigma_{\mathrm{eff}}}\,\tilde{\mathrm{N}}$$

$$\left.\frac{\partial \tilde{\mathrm{N}}}{\partial \mathrm{T}}\right|_{k}^{n+1} \;=\; \frac{3}{2\,\sigma_{\mathrm{eff}}}\left(\mathbf{P}_2\,\mathbf{L} - \frac{2}{3}\,\tilde{\mathrm{N}}\,\tilde{\mathrm{N}}^{T} \right) \tag{31}$$

substituting Eq. (31) and Eq. (31) in Eq. (30)

$$\bar{\mathbf{K}} \;=\; \mathbf{I} \;+\; 2\mu\,\Delta t \left[\left(\frac{\partial \dot{\epsilon}^{vp}}{\partial \sigma_{\mathrm{eff}}} \;-\; \frac{\dot{\epsilon}^{vp}}{\sigma_{\mathrm{eff}}} \right) \mathbf{L}^{-1}\,\tilde{\mathrm{N}}\,\tilde{\mathrm{N}}^{T} \;+\; \frac{3\,\dot{\epsilon}^{vp}}{2\,\sigma_{\mathrm{eff}}}\,\mathbf{P}_2 \right]_{k}^{n+1} \tag{32}$$

The iterative form of the stress update becomes

$$\mathrm{T}_{k+1}^{n+1} \;=\; \mathrm{T}_{k}^{n+1} \;+\; d\mathrm{T} \tag{33}$$

Finally, the consistent tangent elasto-viscoplastic operator can be derived directly from the integration scheme and is defined as

$$\mathbf{C}^{ep} \;=\; \bar{\mathbf{K}}^{-1}\,\mathbf{C} \tag{34}$$

Once $\mathbf{C}^{ep}$, and T_{i}^{n+1} are determined, the tangent stiffness matrix and the residual vector can be computed using Eq. (20). It is well known that the Newton-Raphson method exhibits its fast rate of convergence and stability only when the trial is close to the solution. In reality, for highly nonlinear problems the trial solution may be far away from the real solution. Thus, by applying a full step-size correction in the iteration, the updated vector may actually be detrimental to the solution, causing convergence difficulties. Therefore, a line-search algorithm is implemented within each iteration to overcome the divergence difficulty. The line-search algorithm is well explained in Nallathambi et al. (2009).

4 Thermomechanical Simulation

In this work, a cylindrical extrusion billet of radius 100 mm is considered for the study which is schematically represented in Fig. 1. Due to the rotational symmetry, only a rectangular domain is considered for the analysis. Further, the x-axis represents the radial direction and the y-axis represents the axial direction and axis of symmetry. The height of mold is taken as 60 mm. The billet height is considered as a function of time and increases in the y direction according to the casting speed. The initial height of the billet is taken as 10 mm with 2 rows of elements which is the computational domain for the first time step. For the next time step, an additional row of liquid elements is added in the y direction. The element growth in the y direction represents the liquid feeding from the furnace. Fig. 2 shows the computational domain at time t and $t + \Delta t$.

The thermal boundary of the billet is divided into five regions which are non-overlapping. Γ_1 represents the symmetry axis where the heat flux leaving in the normal direction is considered as zero, i.e., insulated BC. Γ_1 extends along with the element growth. Γ_2 is the temperature described essential BC which mimics the liquid feeding. Γ_2 is assigned to the melt temperature which does not vary with time. The size of the Γ_2 BC is fixed but it shifts in the positive y-direction along the element growth as shown in Fig. 2. The interaction of the billet with the bottom block is represented through Γ_3 convection BC. The size of Γ_3 is fixed and the HTC (heat transfer coefficient) is assumed to vary with temperature. The air gap formation and water intrusion cases are imposed on the HTC. Fig. 3(a) shows the bottom block HTC as a function of temperature which is taken from Williams et al. (2003). Γ_4 represents the primary mold cooling regions with a fixed length, which moves upward in the y-direction during the element growth. This boundary condition is always referred from the top of the melt. Fig. 3(b) shows the bottom block HTC as a function of the air gap which is taken from Drezet et al. (2000). A small portion of size 10 mm is added along with the mold BC which represents the gap between the mold and water impingement

zone known as air cooling zone. The HTC of this air cooling zone is taken as 50 W/m^{2}K. The temperature of the mold is taken as 100^{o}C. The secondary water cooling zones are represented by Γ_5 which changes its size during the element growth. Generally, in the simulation of DC casting, the secondary cooling boundary is the most complicated one due to the high number of controlling parameters such as water flow rate, surface temperature, cooling water quality, etc. In this work, the secondary cooling HTC is taken from Williams et al. (2003) and shown in Fig. 4.

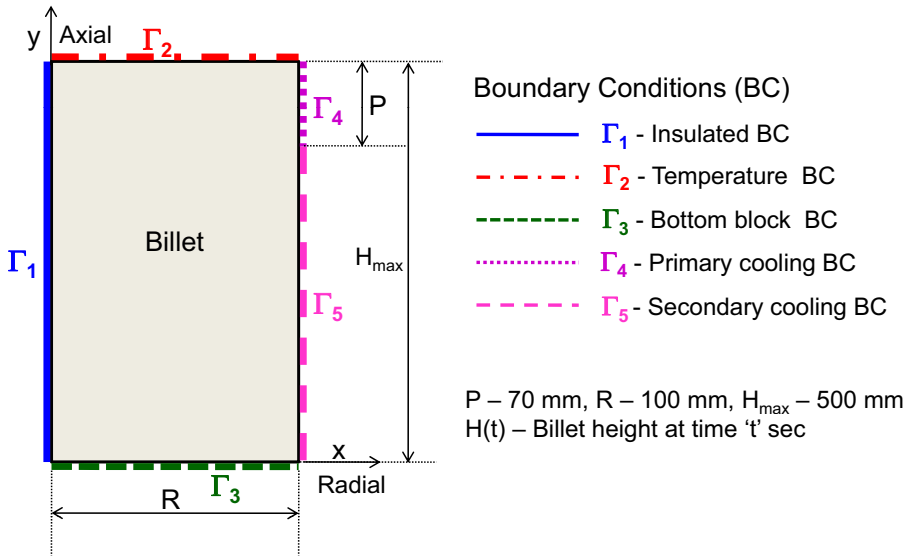

Figure 1: Computational domain of DC casting billet with thermal and mechanical boundary conditions

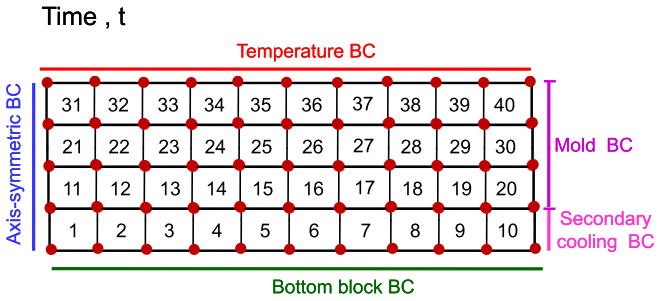

(a) At time t

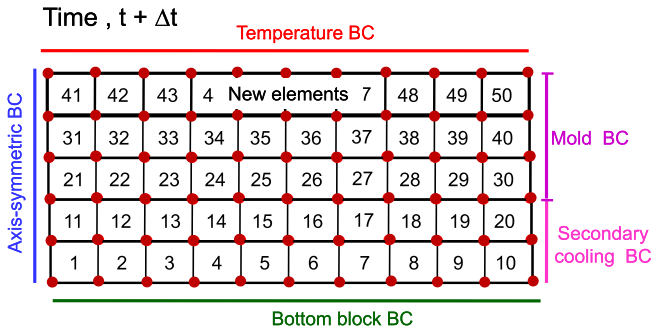

(b) At time $t + \Delta t$

Figure 2: Computational domain of DC casting billet at time t and $t + \Delta t$

The mechanical boundary conditions can be classified into three: (a) axisymmetric boundary conditions are assigned on the Γ_1 regions, (b) to avoid the rigid body motion, the origin of the billet is fixed, and (c) to avoid the penetration of the billet on bottom block, Γ_3 is fixed for the first 15 seconds and then released.The air gap between the bottom block and the billet can be considered as the vertical displacement of the nodes on Γ_3 regions.The computational domain includes the liquid metal, the mushy zone, and the solid part. The material is assumed to be

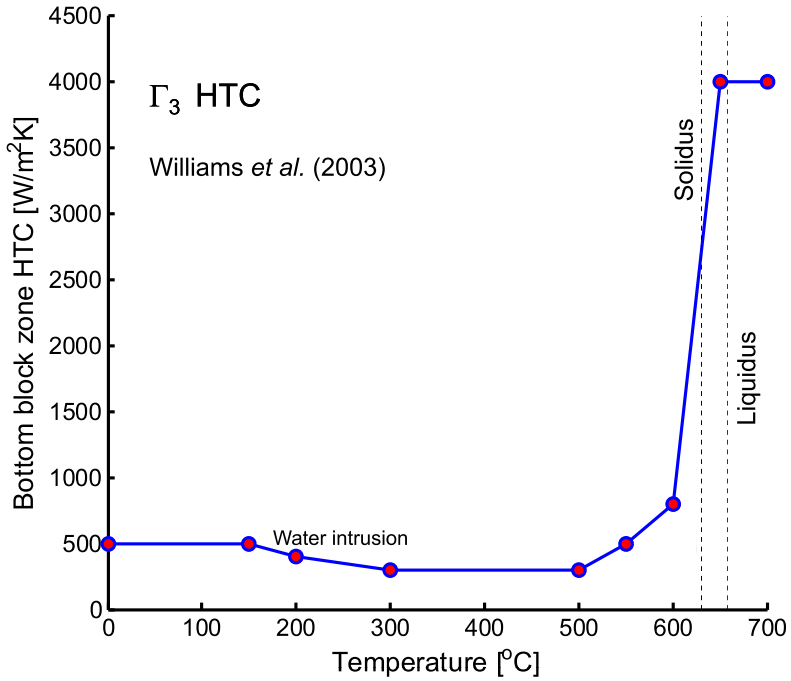

(a) Bottom block boundary HTC Williams et al. (2003)

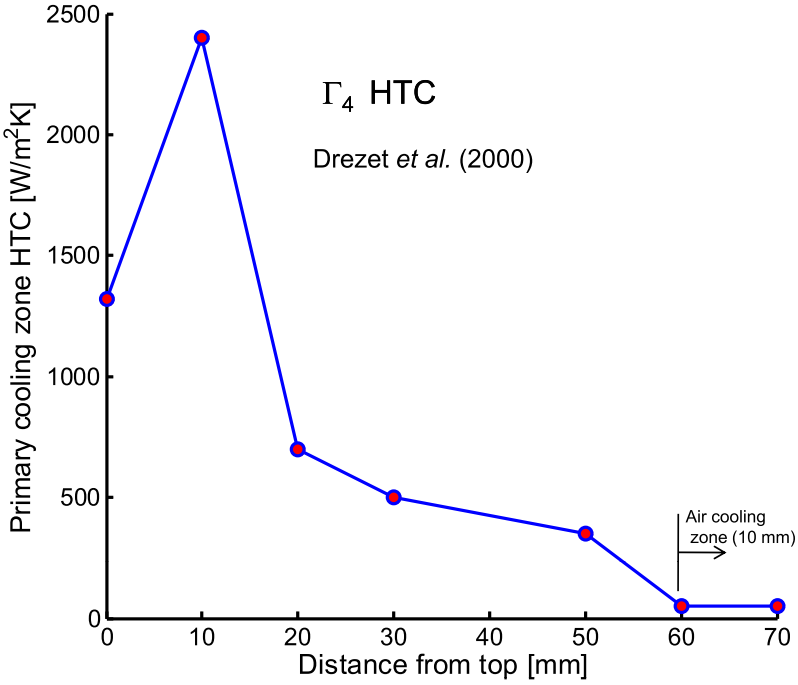

(b) Mold boundary HTC Drezet et al. (2000)

Figure 3: Bottom block and mold boundary HTCs

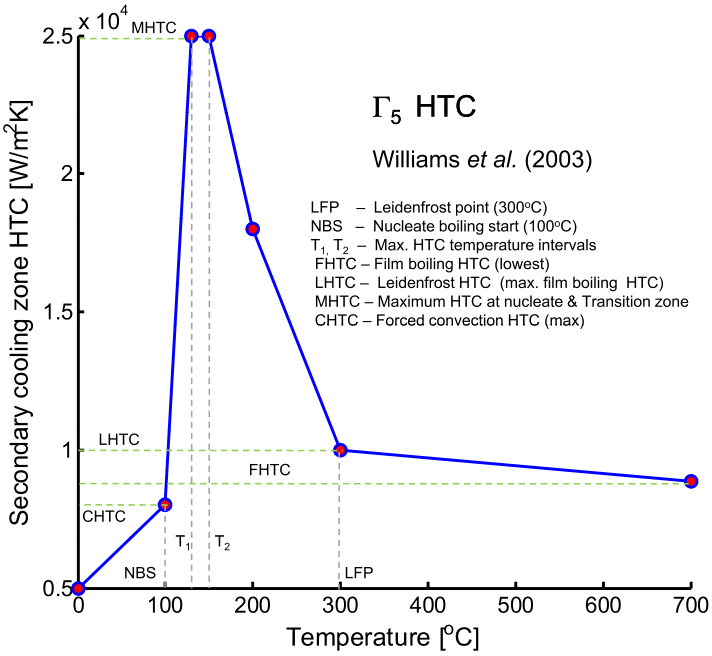

Figure 4: Secondary water cooling region HTC (Williams *et al.* 20003) as a function of temperature

an AA1201 alloy. The thermophysical and thermomechanical properties of the alloy are taken from Drezet and Rappaz (1996).

A constant casting speed of 120 mm/min is investigated.The evolution of radial, axial, and circumferential stresses at the center and the subsurface (90 mm from center in the radial direction) of the billet are plotted in Fig. 5. Near the bottom of the billet, the influences of boundary condition is very high. Therefore, the cross-section considered for the analysis is taken at 50 mm from the bottom. Due to the symmetry, the radial and circumferential components of stresses are equal at the center. In the center, all the stress components are tensile in nature. However, near the subsurface, the axial and circumferential stresses are compressive. It can be seen that stresses become constant after certain time. The higher value of tensile stresses near the center of the billet can easily open the existing cracks.

The circumferential stress and circumferential viscoplastic strain as a function of temperature are plotted in Fig. 6. Three locations are selected such as the center of the billet at start-up phase (1), center of the billet at pseudo steady state (2), and subsurface of the billet at pseudo steady state (3). Until the coherency temperature, there is no accumulation of stress and viscoplastic strain at all the locations. From the coherency to the solidus, the location (1) which corresponds to the start-up phase, the stress and viscoplastic strain are tensile in nature. However for the location (2) and (3), the nature of stress and strain are compressive in the mushy state. Below the solidus temperature, the nature of stress and strain at the locations (1) and (2) are tensile but for the location (3), it is compressive. Overall, the start-up phase stress and strain are higher when compared to the steady state for all temperatures. This tensile nature of stress and strain in the mushy zone is the most favorable situation for the development of hot tear.

The contours of radial, axial, and circumferential stresses during the steady state casting are shown in Fig. 7. It can be perceived that the stresses start developing in the mushy zone in the vicinity of the coherency. The radial stress is tensile at all positions except a smaller region nearby the water impingement. The axial and circumferential stresses are compressive close to the edge and tensile in the center of the billet. In the water impingement zone, the axial stress is relatively higher and tensile in nature. Nearby the solidus, the stress state is tensile which is in good agreement with Suyitno et al. (2004).

The contours of radial, axial, and circumferential viscoplastic strains during the steady state casting are shown in Fig. 8. The radial viscoplastic strain is compressive near the subsurface of the billet and tensile in the center. In contrast to the axial stress, the axial viscoplastic strain is compressive near the center and tensile at the edge which is in good agreement with Suyitno et al. (2004). The circumferential viscoplastic strain is compressive near the edge of the billet and tensile in the center of the billet. The radial and circumferential viscoplatic strains in the

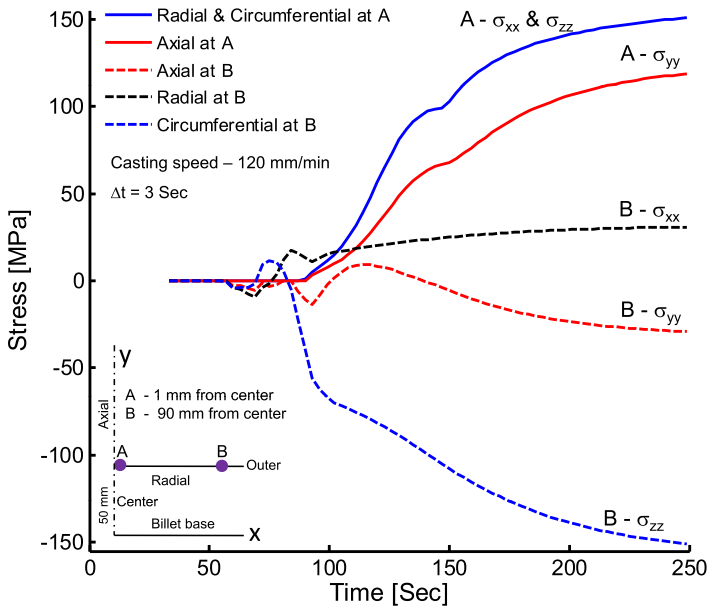

Figure 5: Casting speed 120 mm/min: evolution of stress at center and a radial distance of 90 mm (50 mm from bottom)

mushy state close to the solidus and nearby the center are tensile whereas it becomes compressive near the edge. However, the axial viscoplastic strain behaves oppositely.

5 Influence of Casting Speed

The influence of casting speed is studied by considering six different casting speed profiles which are given as a function of the billet height as shown in Fig. 9. In all the cases, during the steady state condition, the casting speed is maintained constant. However, the start-up phase casting speed is different for all the cases. The circumferential component of stress and viscoplastic strain at the solidus temperature vs. billet height at the center are shown in Fig. 10 for the different casting profiles. In all cases, the maximum tensile stress occurs at a height of 48–54 mm which corresponds to the start-up phase. However, for the cases 5 and 6, the stress becomes compressive after the peak and remains compressive during the steady state. In contrast to case-5 and case-6, in all other cases, the nature of steady state stress is tensile which is favorable for the growth of the existing crack or hot tear. For case-3, not only in the start-up phase, during the steady state hot cracks may form due to relatively higher tensile stress. The strain concentration nearby the bottom block zone is very high. Therefore, for plotting the viscoplastic strain, 35 mm from bottom is omitted (Fig. 10(b)). For the cases 1 to 4, the start-up phase strains are tensile and then remain tensile for the cases 3 and 4 during the steady state. The steady state strains are compressive for the cases 1, 2, 5, and 6. In contrast to the stress behavior near the mushy zone during the start-up phase, the viscoplastic strains are compressive for the cases 5 and 6. Finally, the rating is same as before.

6 Influence of Secondary Cooling

At present, the influence of secondary cooling is not well understood in the DC casting research community. This is mainly due to the insufficient experimental techniques to describe the boiling curve. Apart from the experimentations, the inverse nature of this problem increases the computational difficulty. The exact relation between the major controlling variables such as the water flow rate, water quality, surface roughness, thermo physical properties of the casting materials is not yet well established. Therefore, a theoretical study is conducted to establish the influence of secondary cooling. To achieve this motive, the previously mentioned secondary HTC is multiplied by a factor which varies from 0.5–2 with an increment of 0.5. The resulting HTC profiles are shown in Fig. 11. Here, it should be noted that the Leidenfrost point, maximum HTC temperature intervals, and nucleate boiling start temperature are not changed. Only, the existing HTC profile is allowed to shrink or enlarge by a factor. A constant casting speed of 120 mm/min is employed. Other casting conditions are the same as before. The case-B corresponds to a factor of 1 which is the standard case because the results are already discussed in the above section.

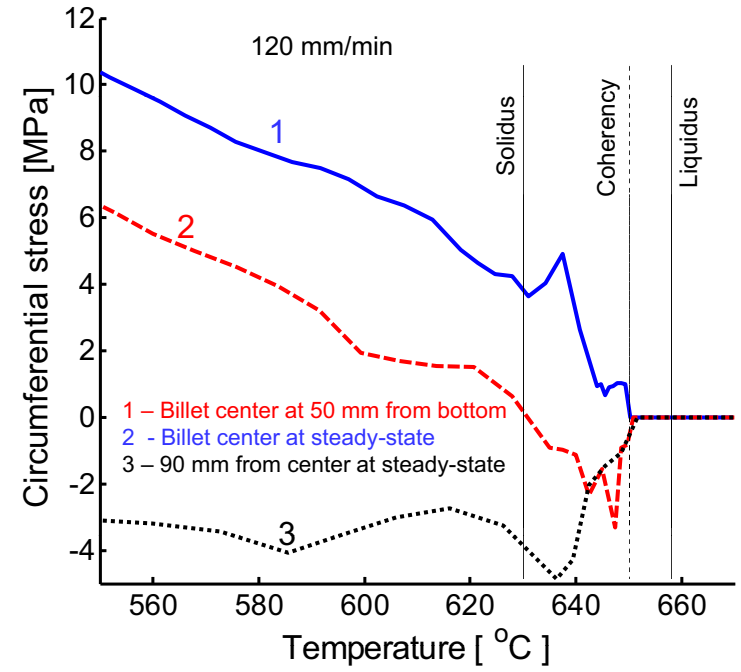

(a) Circumferential stress

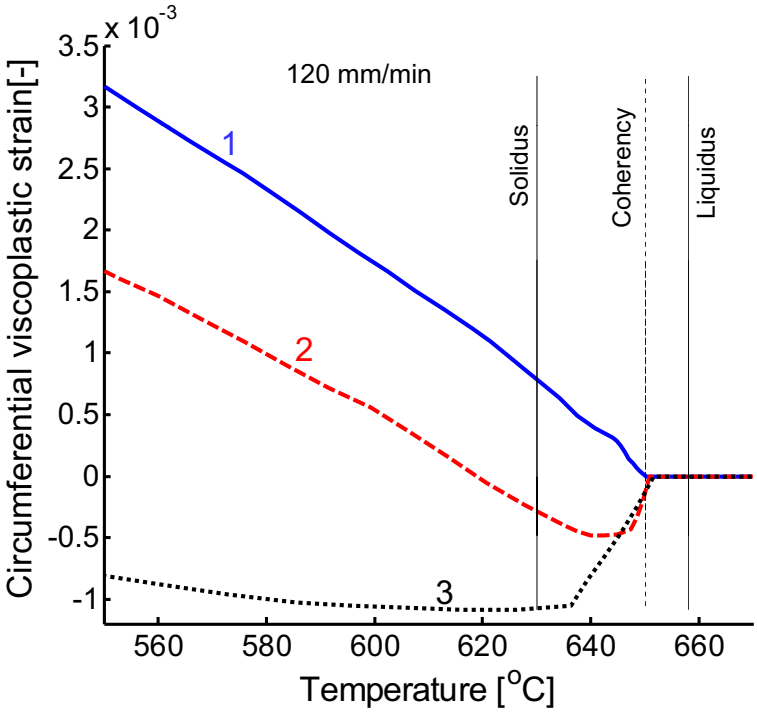

(b) Circumferential viscoplastic strain

Figure 6: Casting speed 120 mm/min: cirumferential stress and viscoplastic strain as a function of temperature

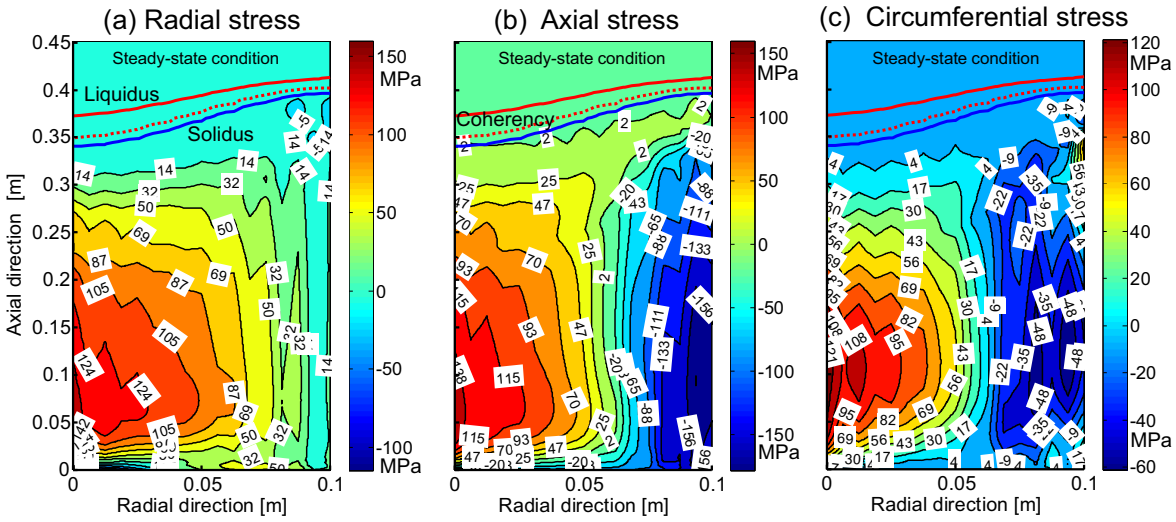

Figure 7: Casting speed 120 mm/min: stress contours at pseudo steady state

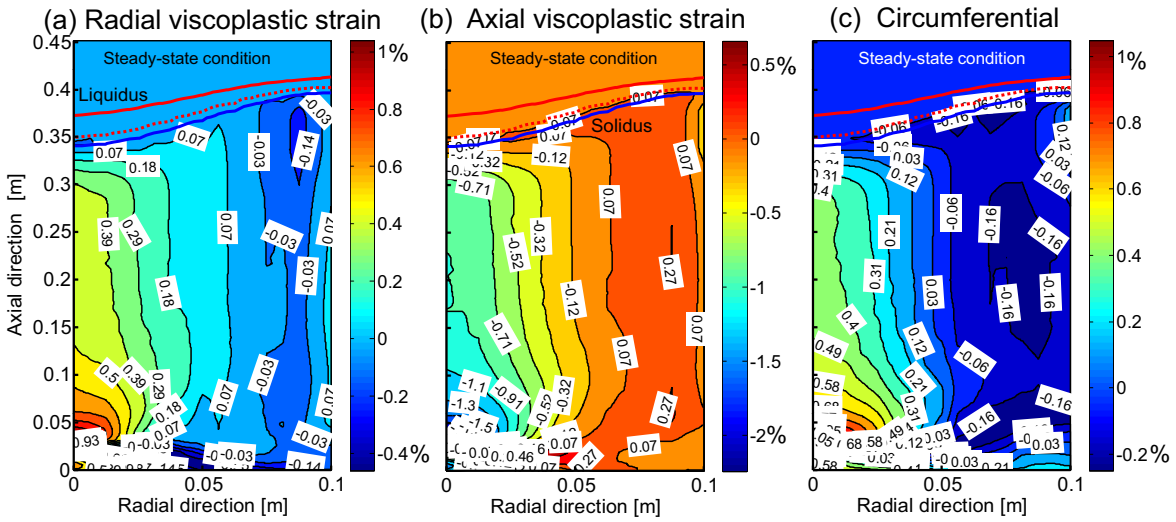

Figure 8: Casting speed 120 mm/min: viscoplastic strain contours at pseudo steady state

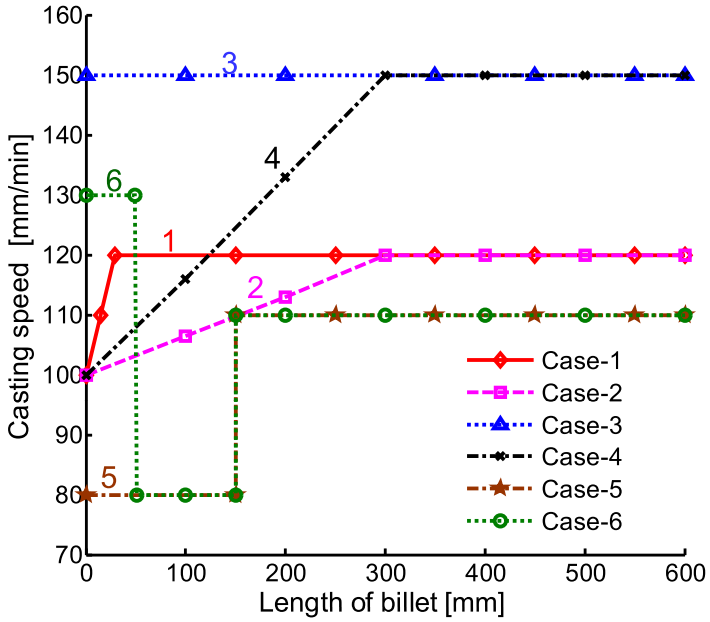

Figure 9: Casting speed profiles vs. length of billet

The evolution of stresses during the start-up phase is compared for case-A and case-D as shown in Fig. 12. Two locations at the start-up phase are selected such as the center and subsurface at 90 mm from center. In both locations, all components of stresses are lower for case-A than case-D. The circumferential component of stress is considerably reduced in case-A when compared to axial and radial components. The axial stress at the subsurface changes its nature from tensile to compressive in case-D, but surprisingly in case-A the nature of stress is monotonically compressive. Generally, during the time of water start striking, the axial stress becomes tensile and in later stages it turns into compressive. This behavior is missing in case-A. Therefore, the chances of quench crack formation at the surface is lower for case-A.

The circumferential stress and viscoplastic strain as a function of temperature is shown in Fig. 13 for three different locations such as the center at 50 mm from bottom, the center at steady state, and the subsurface of 90 mm from center at steady state. For case-D, only during the start-up phase, the stresses are higher, but during the steady state the stresses are lower than case-A. Further, in case-A, the subsurface stress during the steady state turn into tensile at 570^{o}C but in case-D, it remains compressive. If the stress is a deciding factor, the chances of developing cold cracks are higher for case-A than case-D. However, the probability of hot tear formation for case-D is higher than case-A. A similar behavior is observed for the viscoplastic strain except the subsurface at steady state where case-D dominates than case-A. The compressive nature of stress and strain are highly preferred to the tensile one at the vicinity of cracks. With this notion, case-D is better than case-A at the center during the steady state, but in the subsurface the situation is complicated due to the opposite nature of stress and strain.

The complicated behavior of stress and strain restricts the possibilities to make any such conclusions. Further the complexity increases if the axial component of stress and strain are taken into account. This study reveals the fact that through the controlled cooling, the pattern of evolution of stress and strain can be changed. With a proper optimization, it may be possible to reduce the probability of hot or cold cracking. At this moment, it is not possible to conclude which cooling strategy is the better one.

7 Summary and Conclusions

The start-up and steady state phases of DC casting is modeled. It is found that all components of stresses and viscoplastic strains are maximum at the billet center. Further, the nature of stresses and strains at the center are tensile and its maximum occurs during the start-up phase except the axial viscoplastic strain. Tensile nature of stress and strain at the end of the solidification is a favorable situation for the development of hot tears. From the above observations, it can be concluded that the start-up phase is the most critical phase in DC casting. And also the hot tearing most likely occurs during the start-up phase than the steady phase. It is found that the vulnerability

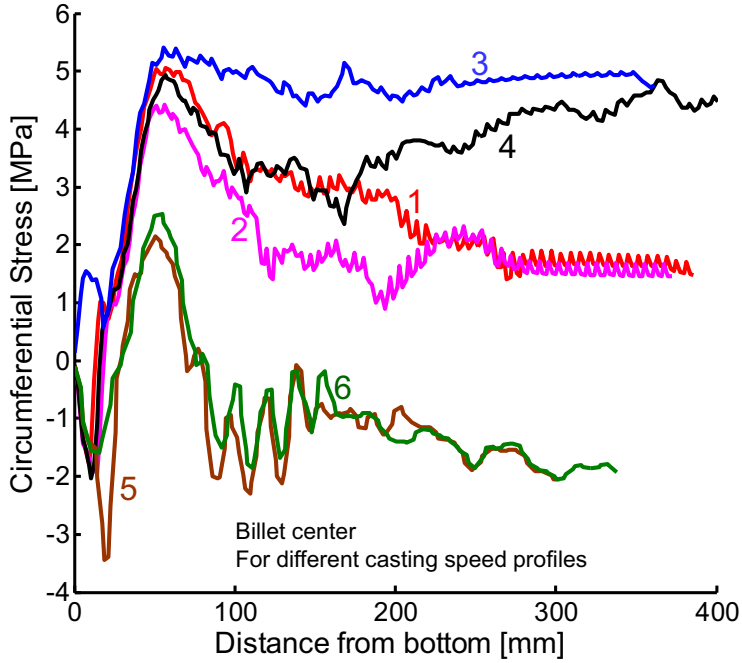

(a) Circumferential stress

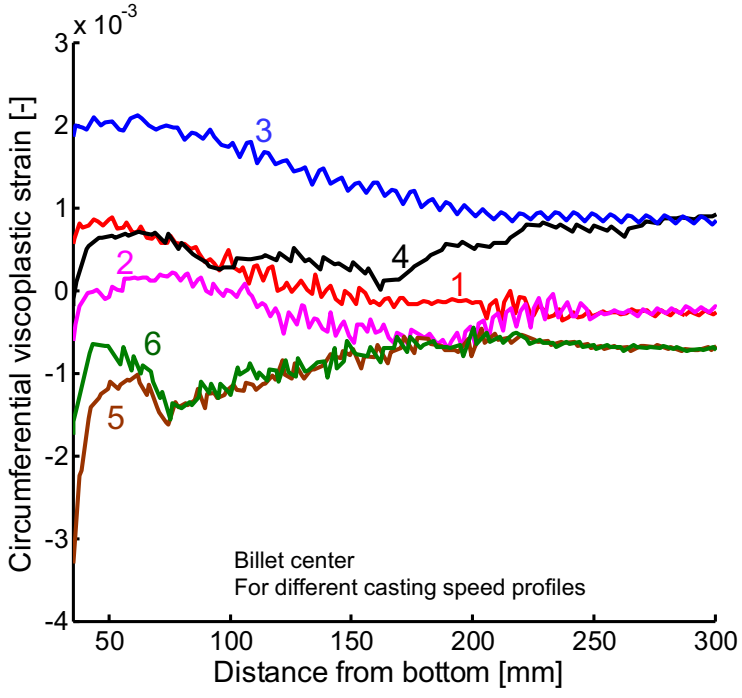

(b) Circumferential viscoplastic strain

Figure 10: Influence of casting speed profile: circumferential stress and viscoplastic strain at solidus temperature as a function of distance from bottom of the billet

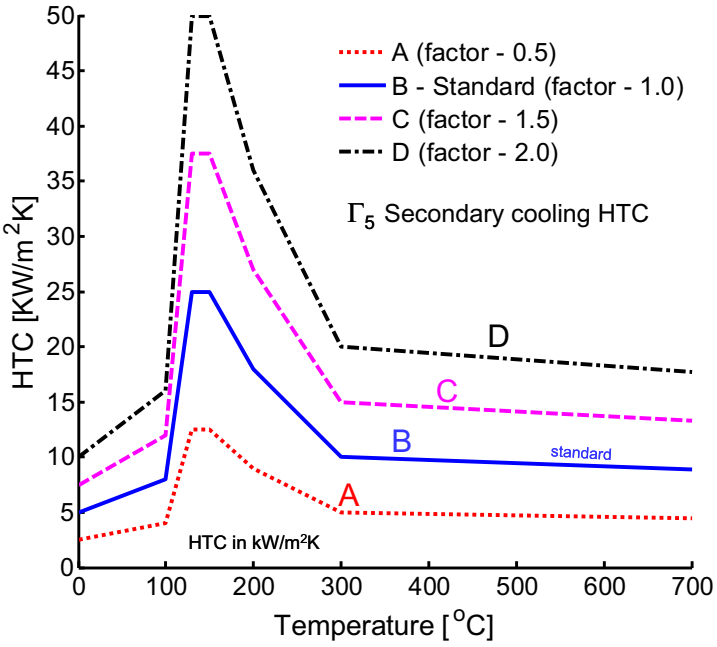

Figure 11: Influence of secondary cooling: different HTC profiles

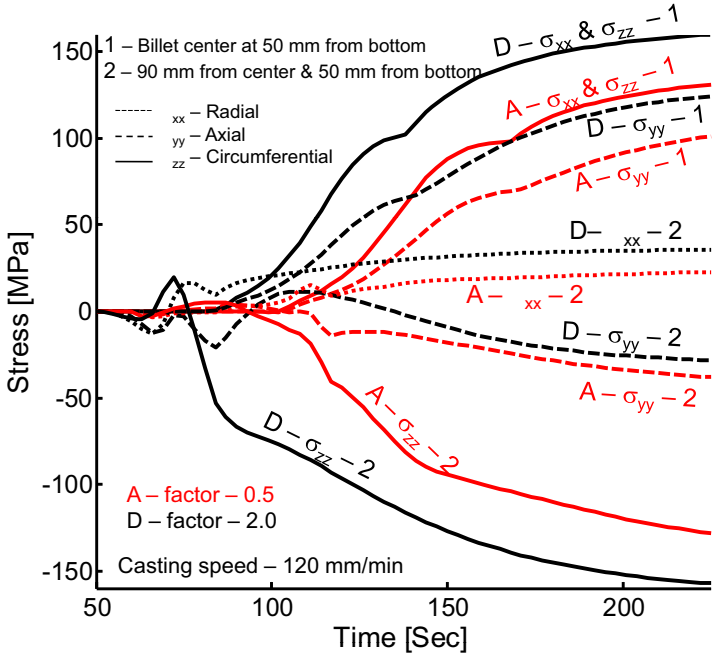

Figure 12: Influence of secondary cooling profile: evolution of stress at center and a radial distance of 90 mm (50 mm from bottom)

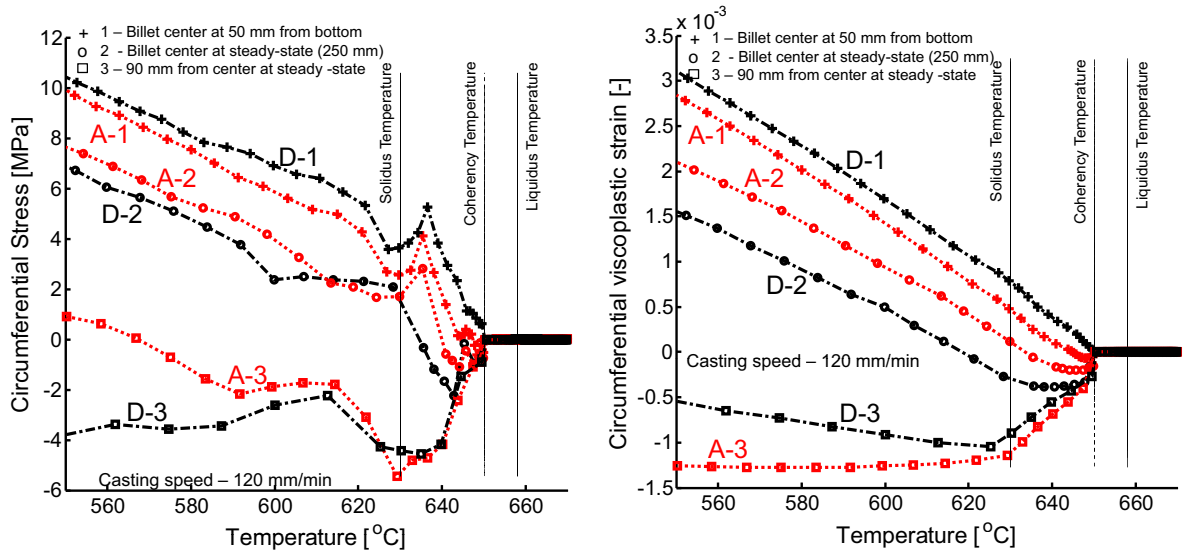

(a) Circumferential stress

(b) Circumferential viscoplastic strain

Figure 13: Influence of secondary cooling profile: circumferential stress and viscoplastic strain as a function of temperature

of the start-up phase can be minimized by a proper ramping procedure. Further, ramping delays the time and increases the billet height to reach the steady state. Stresses and strains in the mushy zone increase with increasing casting speed and they are maximum in the start-up phase. Ramping reduces the start-up phase stresses and strains. Reduced secondary cooling reduces the start-up phase stresses and strains. However, during the steady state, increased cooling decreases the stresses and strains in the mushy. Therefore, the secondary cooling has to be decreased to reduce the chances of hot crack formation during the start-up phase. Similarly for the steady state, an increase in secondary cooling reduces the hot crack development. Even though the pattern of stress and strain evolution changes for different cooling strategies, due to the complex nature of residual stresses and strains, there is no specific conclusion made in this regarding

References

Celentano, D.; Orate, E.; Oller, S.: A temperature-based formulation for finite element analysis of generalized phase-change problems. *International Journal for Numerical Methods in Engineering*, 37, (1994), 3441–3465.

Drezet, J. M.; Rappaz, M.: Modeling of ingot distortions during direct chill casting of aluminum alloys. *Metallurgical and Materials Transactions A: Physical Metallurgy and Materials Science*, 27, (1996), 3214–3225.

Drezet, J. M.; Rappaz, M.; Grun, G. U.; Gremaud, M.: Determination of thermophysical properties and boundary conditions of direct chill-cast aluminum alloys using inverse methods. *Metallurgical and Materials Transactions A: Physical Metallurgy and Materials Science*, 31, (2000), 1627–1634.

Fachinotti, V. D.; Cardona, A.; Huespe, A. E.: A fast convergent and accurate temperature model for phase-change heat conduction. *International Journal for Numerical Methods in Engineering*, 44, (1999), 1863–1884.

Fjær, H. G.; Mo, A.: ALSPEN-A mathematical model for thermal stresses in direct chill casting of aluminum billets. *Metallurgical Transactions B*, 21, (1990), 1049–1061.

Katgerman, L.; Flood, S. C.; Langille, A. H.: Modelling of D.C. casting of aluminium alloys. *Production, Refining, Fabrication and Recycling of Light Metals*, pages 96–110.

Magnin, B.; Maenner, L.; Katgerman, L.; Engler, S.: Ductility and rheology of an Al-4.5% Cu alloy from room temperature to coherency temperature. *Materials Science Forum*, 217-222, (1996), 1209–1214.

M'Hamdi, M.; Benum, S.; Mortensen, D.; Fjær, H. G.; Drezet, J. M.: The importance of viscoplastic strain rate in the formation of center cracks during the start-up phase of direct-chill cast aluminum extrusion ingots. *Metallurgical and Materials Transactions A: Physical Metallurgy and Materials Science*, 34, (2003), 1941–1952.

Nallathambi, A. K.; Specht, E.; Bertram, A.: Computational aspects of temperature based finite element technique for the phase-change heat conduction problem. *Computational Materials science*, 47, (2009), 332–341.

Suyitno; Kool, W. H.; Katgerman, L.: Finite element method simulation of mushy zone behavior during direct-chill casting of an Al-4.5 pct Cu alloy. *Metallurgical and Materials Transactions A: Physical Metallurgy and Materials Science*, 35-A, (2004), 2917–2926.

Williams, A. J.; Croft, T. N.; Cross, M.: Modeling of ingot development during the start-up phase of direct chill casting. *Metallurgical and Materials Transactions B: Process Metallurgy and Materials Processing Science*, 34, (2003), 727–734.

Address: P. Pavan Kumar, A. K. Nallathambi, E. Specht, A. Bertram, Otto von Guericke University Magdeburg, 39106 Magdeburg, Germany
email: pavan.penumakala@st.ovgu.de,ashok.nallathambi@ovgu.de